D-Shaped Tellurite Photonic Crystal Fiber Hydrogen and Methane Sensor Based on Four-Wave Mixing With SPR Effect

Hai LIU[1,2*], Bo WU[1], Cong CHEN[1], Benlei ZHAO[1], Xu ZHANG[1], and Hancheng ZHANG[1]

[1]*School of Information and Control Engineering, China University of Mining and Technology, Xuzhou 221116, China*
[2]*Engineering Research Center of Intelligent Control for Underground Space (Ministry of Education), China University of Mining and Technology, Xuzhou 221116, China*

[*]Corresponding author: Hai LIU E-mail: sieeoe@cumt.edu.cn

Abstract: A new D-shaped tellurite photonic crystal fiber sensor based on the four-wave mixing (FWM) effect with the surface plasmon resonance (SPR) effect is designed and optimized. The substrate of the D-shaped photonic crystal fiber (D-PCF) is tellurite glass, and the polished surface is plated with the gold film and hydrogen gas-sensitive film. An air hole of the inner cladding, which is plated with the gold film and methane gas-sensitive film, is selected as the second sensing channel to simultaneously measure the concentration of hydrogen and methane. Based on the four-wave mixing, the wavelength shifts of the Stokes and anti-Stokes spectra resulting from the variation of the gas concentration can be used to accurately detect the concentrations of methane and hydrogen. Meanwhile, it is found that the SPR effect can increase the wavelength shifts, which means the sensitivity of methane and hydrogen augment. After parameter optimization, the maximum sensitivities of methane and hydrogen are 4.03 nm/% and –14.19 nm/%, respectively. Both the linearities are up to 99.9%. The resolution of methane is 1.25×10^{-2}% and hydrogen is 7.14×10^{-3}%. Moreover, the fiber length of this sensor is only 20 mm, which is conducive to the construction of a compact or ultra-compact embedded FWM fiber sensor.

Keywords: Four-wave mixing; surface plasmon resonance; D-shaped photonic crystal fiber; gas sensing

Citation: Hai LIU, Bo WU, Cong CHEN, Benlei ZHAO, Xu ZHANG, and Hancheng ZHANG, "D-Shaped Tellurite Photonic Crystal Fiber Hydrogen and Methane Sensor Based on Four-Wave Mixing With SPR Effect," *Photonic Sensors*, 2023, 13(1): 230121.

1. Introduction

Based on the porous structure of photonic crystal fibers, surface plasmon resonance (SPR) produced by filling metal rods or coating metal films has recently become a hot spot in the field of optical fiber sensors. In particular, researches on the SPR coated with the metal film on the polished surface of the D-shaped photonic crystal fiber (D-PCF) are more attractive, including the refractive index [1], methane [2], temperature [3], magnetic field [4], strain, [5] and biochemistry [6] sensors. Most of the above studies are conducted by the loss spectrum which has some disadvantages. It can only provide one degree of freedom, which needs to be combined with other methods or special PCF structures, such as the Sagnac interference [3], directional coupling [7], or side-hole structure [8] to achieve dual-parameter sensing. At present, the detection of the gas concentration is often limited by detecting the sensitivity and cross-sensitivity. An even greater obstacle is the inability to accurately detect specific

Received: 16 July 2021 / Revised: 29 January 2022

DOI: 10.1007/s13320-022-0655-8
Article type: Regular

gases in mixtures of two or more gases. The four-wave mixing (FWM) effect can solve this problem. The FWM process is accompanied by the annihilation of two photons, resulting in two new photons. Thus, two gain peaks, Stokes and anti-Stokes, are formed, and the Stokes and anti-Stokes peak shifts can provide two independent sensing channels to achieve dual-parameter sensing by a sensitivity demodulation matrix. Since the FWM is very sensitive to optical fiber dispersion, the method combined with the SPR effect can obtain high sensitivity. In 2018, Nallusamy *et al*. [9] designed a D-shaped PCF-SPR sensor to simultaneously measure the temperature and salinity of seawater by using the FWM effect. The salinity sensitivity and temperature sensitivity are 1.6 nm/% (kg/kg) and 12.31 nm/℃, respectively. Although gas-sensing has not yet been reported, the FWM effect combined with the SPR effect has good application prospects in the multi-gas detection field.

Most PCF sensors use silica as the substrate, and the transmission window of the quartz fiber is 0.38 μm – 2.3 μm. When the wavelength of the transmitted light wave exceeds 2.3 μm, the transmission loss will increase sharply [10]. The silica has a lower nonlinear coefficient, which limits its application in near-infrared and mid-infrared areas. Therefore, tellurite glass has attracted wide attention due to its wider infrared transmission range, greater nonlinear refractive index, insulation constant, damage threshold, and better third-order nonlinear optical performance [11, 12]. The nonlinear coefficient of the tellurite PCF is more than ten times that of the silicon substrate, which makes it easier to meet the phase matching conditions to generate the highly efficient FWM. In 2020, Sun *et al*. [13] realized temperature sensing by using the FWM in the tellurite photonic crystal fiber, and the temperature sensitivity of the sensor was 0.7 nm/℃ at the pumped wavelength of 3550 nm. In the following year, Chen *et al*. [14] realized FWM temperature sensing in the chalcogenide PCF, and the sensitivity was as high as 2.32 nm/℃ in the range of –80℃ to 45℃, with a pump wavelength of 8510 nm.

However, there are few reports in the field of gas sensing, especially in hydrogen sensing. At present, the main methods are Bragg grating and Saganc interference, which are complex and have low sensitivity [15, 16, 20]. In conclusion, as both methane and hydrogen are flammable and explosive gases, it is essential to detect their concentrations. Therefore, it is necessary to design a sensing device that can detect the concentrations of methane and hydrogen simultaneously to achieve higher sensitivity and better accuracy.

In this paper, a new D-shaped PCF-SPR sensor based on the FWM effect is proposed and optimized. Here, we adopt tellurite glass as the substrate and plate the gold film and hydrogen-sensitive film on the polished surface of the D-PCF. Another air hole is selected to be coated with the gold film and methane-sensitive film as the second sensing channel to realize the simultaneous measurement of hydrogen and methane concentrations in mixed gas. The characteristics of the sensor are numerically investigated by using the full vector finite element method under the anisotropic boundary conditions of the perfectly matched layer (PML). When the gas mixture passes through, the refractive index of the gas-sensitive film will change. This will affect the dispersion and nonlinear coefficient of the PCF propagation mode and eventually lead to the shift of the gain peaks of the Stokes spectrum and anti-Stokes spectrum. It is found that the SPR effect enhances the gain peak shifts, which increases the sensitivity of the sensor. After parameter optimization, the final sensitivity of methane can reach 4.03 nm/% and that of hydrogen is as high as –14.19 nm/%. Moreover, the fiber length of this sensor is only 20 mm, which is conducive to the construction of compact or ultra-compact embedded FWM fiber sensors. Meanwhile, it is also applicable

to the study of the concentration of other mixed gases, which has a wide application prospect.

2. Basic theory

The FWM is caused by the third-order nonlinear polarizability $\chi^{(3)}$ of the medium. Degenerate four-wave mixing (DFWM) is a special form of the FWM, in which two photons at the same frequency annihilate to produce two new photons, namely Stokes photon and anti-Stokes photon. To understand the sensing mechanism of the DFWM, the Raman effect, self-steepening effect, and linear loss can be ignored to obtain the following modified nonlinear Schrödinger equation (MNLSE), as shown in (1) [17], where A is the normalized light pulse amplitude, z is the propagation distance, t is time, β_n is the nth order propagation constant, and γ is the nonlinear coefficient. Here, n_2 is the nonlinear refractive index of the fiber substrate materials, and A_{eff} is the effective mode field area at the pump wavelength(λ_0).

$$\frac{\partial A}{\partial z}+\sum_{n=2}^{4}\beta_n\frac{\mathrm{i}^{n-1}}{n!}\frac{\partial^n A}{\partial t^n}-\mathrm{i}\gamma|A|^2A=0 \tag{1}$$

$$\beta_n=\left(\frac{\mathrm{d}^n\beta}{\mathrm{d}\omega^n}\right)_{\omega=\omega_0} \tag{2}$$

$$\gamma=\frac{2\pi}{\lambda}\frac{n_2}{A_{\text{eff}}} \tag{3}$$

$$\kappa=2\sum_{n=2,4,6,\cdots}^{\infty}\frac{\beta_n}{n!}\Omega^n+2\gamma P_0. \tag{4}$$

Only the phase mismatch $\kappa=0$ can produce the significant FWM effect, namely phase-matching. According to the energy and momentum conservation, the phase-matching condition of the FWM is defined as (4) [18], where $\Omega=\omega_s-\omega_0=\omega_0-\omega_i$ is the frequency shift, ω_0 is the pump frequency, and ω_s and ω_i are the Stokes and anti-Stokes frequencies, respectively. It should be noted that β_n is the nth order propagation constant, but only the second-order (β_2) and fourth-order(β_4) propagation constants are the most important factors that affect the FWM, thus, the other higher-order propagation constants can be ignored.

Considering the loss of light waves in the propagation process, the influence of the loss on the gain needs to be considered, so the gain formula is shown as (5) [19]:

$$G_s=\mathrm{e}^{-\alpha L}\left[1+2\left(\frac{\gamma P_0}{g}\right)\sinh^2\left(gL_{\text{eff}}\right)\right] \tag{5}$$

$$g=\sqrt{\left(\gamma P_0\right)^2-\left(\frac{\kappa^2}{4}\right)} \tag{6}$$

$$\alpha=\frac{40\pi}{\lambda\ln 10}\mathrm{Im}\left(n_{\text{eff}}\right)\times10^6(\mathrm{dB/m}) \tag{7}$$

where α is the limit loss, P_0 is the peak power of the pump, L is the length of the optical fiber, g is the gain coefficient, and $L_{\text{eff}}=\left(1-\mathrm{e}^{-\alpha L}\right)/\alpha$ is the effective length. Here, $\mathrm{Im}\left(n_{\text{eff}}\right)$ is the imaginary part of the effective refractive index.

In conclusion, the change of the gas concentration will affect the effective refractive index (n_{eff}) of the PCF, making the parameters γ, β_2, and β_4 vary, and finally leading to the shift of the Stokes and anti-Stokes peaks. Therefore, the concentration of the mixed gas can be detected by establishing a direct relationship between the peak shift of Stokes and anti-Stokes spectra and the concentration of gas.

3. Sensing mechanism and modeling

The cross-section diagram of the proposed D-shaped PCF-SPR sensor is shown in Fig. 1(a). The PCF is microprocessed by the laser etching and optical fiber polishing technology to remove part of the fiber cladding of the cylindrical PCF. The substrate material is tellurite glass, the gold film and hydrogen gas-sensitive film are plated on the polished surface of D-PCF, and another inner cladding air hole is selected to be plated with the gold film and methane gas-sensitive film. Metal films mostly adopt the high-pressure chemical vapor deposition technology (CVD). The specific process is to make gaseous or vapor metal plasma react

chemically by means of high pressure heating and deposit the atomic state on the inner side of air holes and polished surface, thus forming metal coating films. The material of the hydrogen-sensitive film is Pd-WO_3 and is coated on the D-shaped polished surface by the sol-gel scheme [20]. Meanwhile, the methane-sensitive film is made of cryptophane-A and UV(ultra-violet)-cured fluorosiloxane (UVCFS), using the capillary dip-coating technique coated on the metal film surface inside an air hole [21]. However, the plating of the nano-level metal and sensing film in the micron-level air hole of the PCF requires a high technological level. The air hole distance is $\Lambda = 8\ \mu m$, the air hole diameter is $d = 3.2\ \mu m$, and the polishing depth is $h = 9.6\ \mu m$. The thicknesses of hydrogen and methane gas-sensitive films are t_{H_2} and t_{CH_4}, respectively. The thickness of the polished surface gold film is d_{H_2} and the inner cladding gold film is d_{CH_4}. Figure 1(b) shows the experimental setup for the FWM-based D-shaped PCF-SPR sensors. The output polarization state of the pump light is selected by an optical polarization controller (PC) and coupled into the single-mode fiber. The signal light modulated by the PCF is output to the optical spectrum analyzer (OSA) through the multimode fiber (MMF) and the wave pass filter (PF). The MMF combined with a wave pass filter can filter out the residual laser light excited by the pump light source, that is, the background spectrum of the FWM is reduced, and only the FWM signal light is collected [18, 23].

The substrate is made of tellurite glass TeO_2 - ZnO - Na_2O - Bi_2O_3 (TZNB), which has a wider infrared transmission range and a larger nonlinear coefficient. The nonlinear refractive index $n_2 = 5.9\times10^{-19}\ m^2/W$ and the wavelength-dependent refractive index of the material can be described by the Sellmeier formula as shown in (8) [22], where A_1=1.671 9, A_2=1.348 6, A_3=0.621 9, B_1=0.000 466 56, B_2=0.057 46, and B_3=46.725 43. In addition, the thermal optical coefficient of tellurite glass is –6 orders of magnitude, so the quantitative change in the refractive index of the tellurite glass with the temperature can be ignored when calculating the effective refractive index [13].

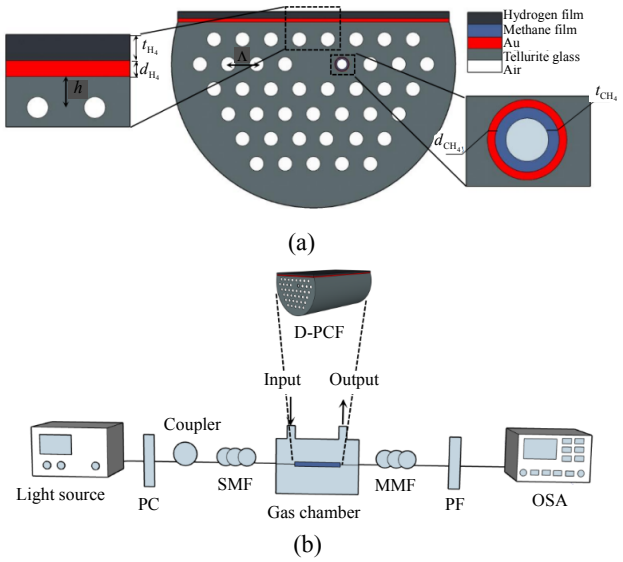

Fig. 1 Schematic diagram of the optical fiber structure and experimental device: (a) cross-section diagram of the D-PCF sensor and (b) diagram of the proposed experimental setup.

Besides, the refractive indexes (RIs) of methane and hydrogen gas-sensitive films are shown in (9) and (10) [8]. The RIs of them are negatively correlated with the concentration in the concentration range of 0% – 3%. The dispersion of gold is described by the Drude-Lorentz model, as shown in (11). Here, ε_{Au} is the permittivity of the gold, $\varepsilon_\infty = 9.75$ is the permittivity at infinite frequency, $\omega_p = 1.36\times10^{16}$ rad/s is the plasma frequency, and $\varepsilon_\tau = 1.45\times10^{14}$ rad/s is the collision frequency.

$$n = \sqrt{1 + \sum_{i=1}^{3} \frac{A_i \lambda^2}{\lambda^2 - B_i}} \tag{8}$$

$$n_{eff} = 1.447\ 8 - 0.003\ 8 C_{CH_4} \tag{9}$$

$$n_{eff} = 1.995 - 0.000\ 67 C_{H_2} \tag{10}$$

$$\varepsilon_{Au}(\omega) = \varepsilon_\infty - \omega_p^2 / (w^2 + i\omega\omega_\tau). \tag{11}$$

4. Simulation analysis and parameter optimization

In this section, the characteristics of the sensor are numerically analyzed by using the full vector finite element method under the anisotropic boundary condition of a perfectly matched layer (PML). We adopt the COMSOL software to simulate the model and analyze the influence of structural parameters on the sensor to determine the optimal structural parameters.

To achieve the efficient four-wave mixing modulation, the optical fiber is required to be equipped with a zero-dispersion wavelength (ZDW) and the dispersion wavelength is as flat as possible. The dispersion curves are influenced by both the thickness of the gold film and the depth of polishing. Next, we will investigate the influence of different gold film thicknesses and polishing depths on the dispersion and select the optimal parameters. The initial parameters of the PCF sensor are selected as $\Lambda = 8\ \mu m$, $d = 3.2\ \mu m$, $t_{H_2} = 300\ nm$, $t_{CH_4} = 260\ nm$, and $L = 20\ mm$. Figures 2(a), 2(b), and 2(c) show the influences of different gold film thicknesses and polishing depths on the optical fiber dispersion. Firstly, the gold film thickness on the polished surface and the polishing depth are kept unchanged. The ZDW blue-shifts as the gold film thickness in the air hole increases. When the gold film thickness is 40 nm ($d_{CH_4} = 40\ nm$), the flatness of the dispersion curve is the best. Secondly, we keep the gold film thickness in the air hole and the polishing depth constant. The ZDW changes little with the augment of the gold film thickness on the polished surface. The flatness of the dispersion curve is the best at the gold film thickness of 40 nm ($d_{H_2} = 40\ nm$). Thirdly, we choose the constant thickness of the gold film and the polishing depth increased from 9.4 μm to 9.8 μm. The impact on the ZDW is also modest. It can be seen that the ZDW is

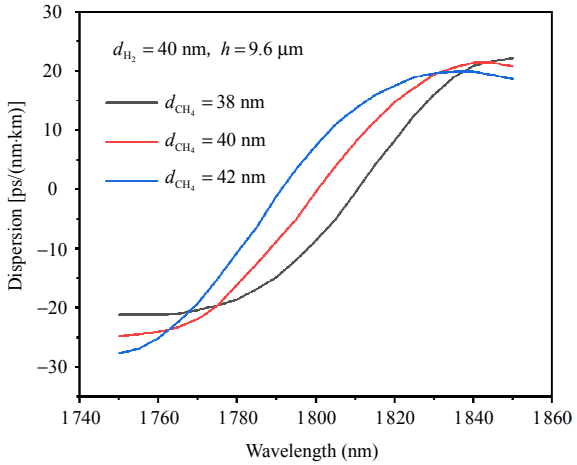

(a)

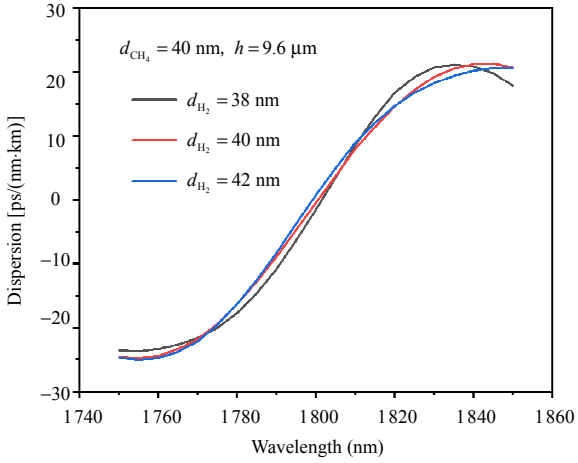

(b)

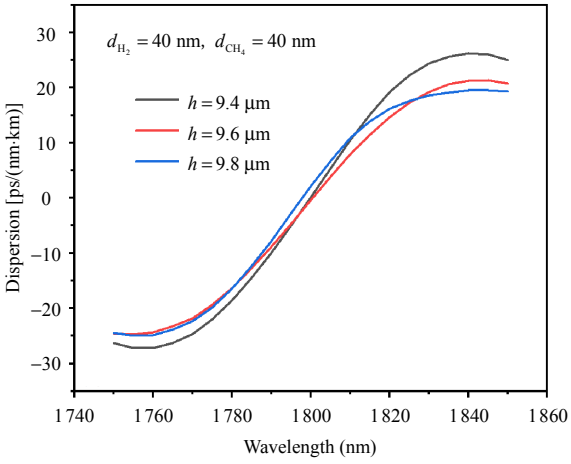

(c)

Fig. 2 Dispersion curves of the gold film thickness: (a) in air hole and (b) on the polished surface; (c) polishing depths.

more sensitive to the gold film thickness in the cladding air hole. The dispersion curve is the flattest when the polishing depth is equal to 9.6 μm. Finally, considering the position of the ZDW and the flatness of the dispersion curve, the optimal parameters $d_{CH_4} = 40$ nm, $d_{H_2} = 40$ nm, and $h = 9.6$ μm are selected, which lead to the ZDW around 1 801 nm.

Under the phase-matching condition, the DFWM can generate Stokes and anti-Stokes sidebands around the pump wavelength with the variation in RI of the measured object. This frequency shift increases with the influence of negative fourth-order dispersion (FOD) in the normal dispersion region [23], namely $\beta_2 > 0$ and $\beta_4 < 0$. Finally, we select 1 798 nm as the pump wavelength and the peak pump power is 5 kW. It is found that with the shortening of the fiber length, the obtained sensitivity is basically unchanged, which is conducive to the construction of compact or ultra-compact embedded FWM sensors. Thus, 20 mm is selected as the fiber length.

Next, the effects of two gas-sensitive film thicknesses on the sensitivity of methane and hydrogen are investigated. Firstly, we keep the methane gas-sensitive film thickness constant at 260 nm, making the hydrogen gas-sensitive film thickness vary from 260 nm to 300 nm with a step length of 20 nm. Then, we change the hydrogen concentration from 0% to 3% with the methane concentration constant at 0%. Figure 3(a) shows the movement of gain peaks corresponding to different hydrogen gas-sensitive film thicknesses when the hydrogen concentration increases from 0% to 2%. It can be seen that the gain peak value decreases with the augment of the hydrogen gas-sensitive film thickness, while the gain peak value basically remains unchanged with the variation of the hydrogen concentration. In order to observe the peak deviation more intuitively, Figs. 4(a) and 4(b) illustrate the specific wavelength shifts of the anti-Stokes and Stokes peaks, respectively. It is obviously shown that each group of the Stokes peaks moves to the short-wave direction, while that of the anti-Stokes peaks moves to the long-wave direction with an increase in the hydrogen gas-sensitive film thickness when the methane gas-sensitive film thickness and the hydrogen concentration are constant. When the hydrogen volume fraction is varied by 0.5%, the anti-Stokes peaks redshift, and the Stokes peaks blueshift, both of the gain peak values decline. Their peak offsets will decrease, but the linearities will augment.

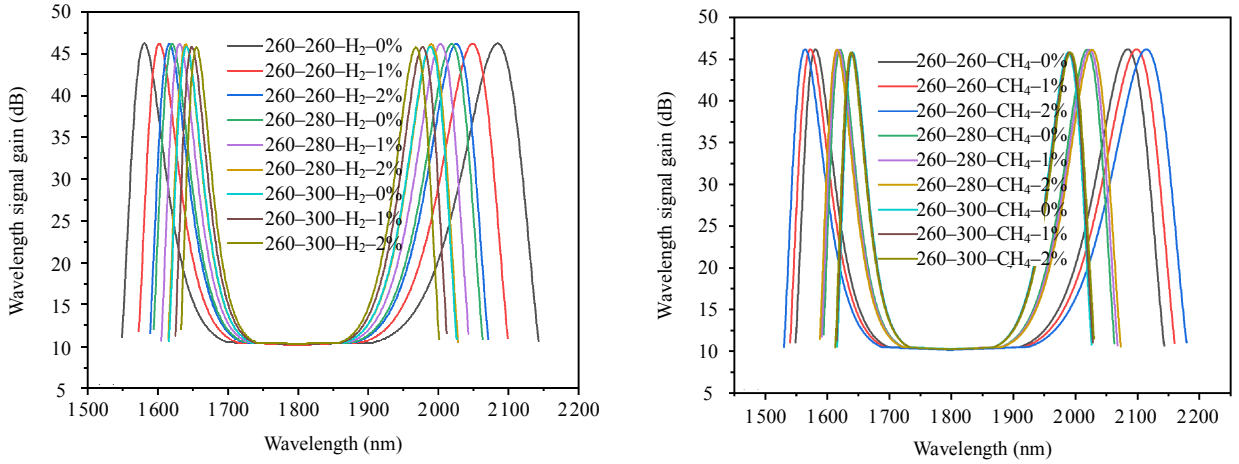

(a) (b)

Fig. 3 Stokes and anti-Stokes gain spectrum curves with the variation of the hydrogen concentration (a) and Stokes and anti-Stokes gain spectrum curves with the variation of the methane concentration (b).

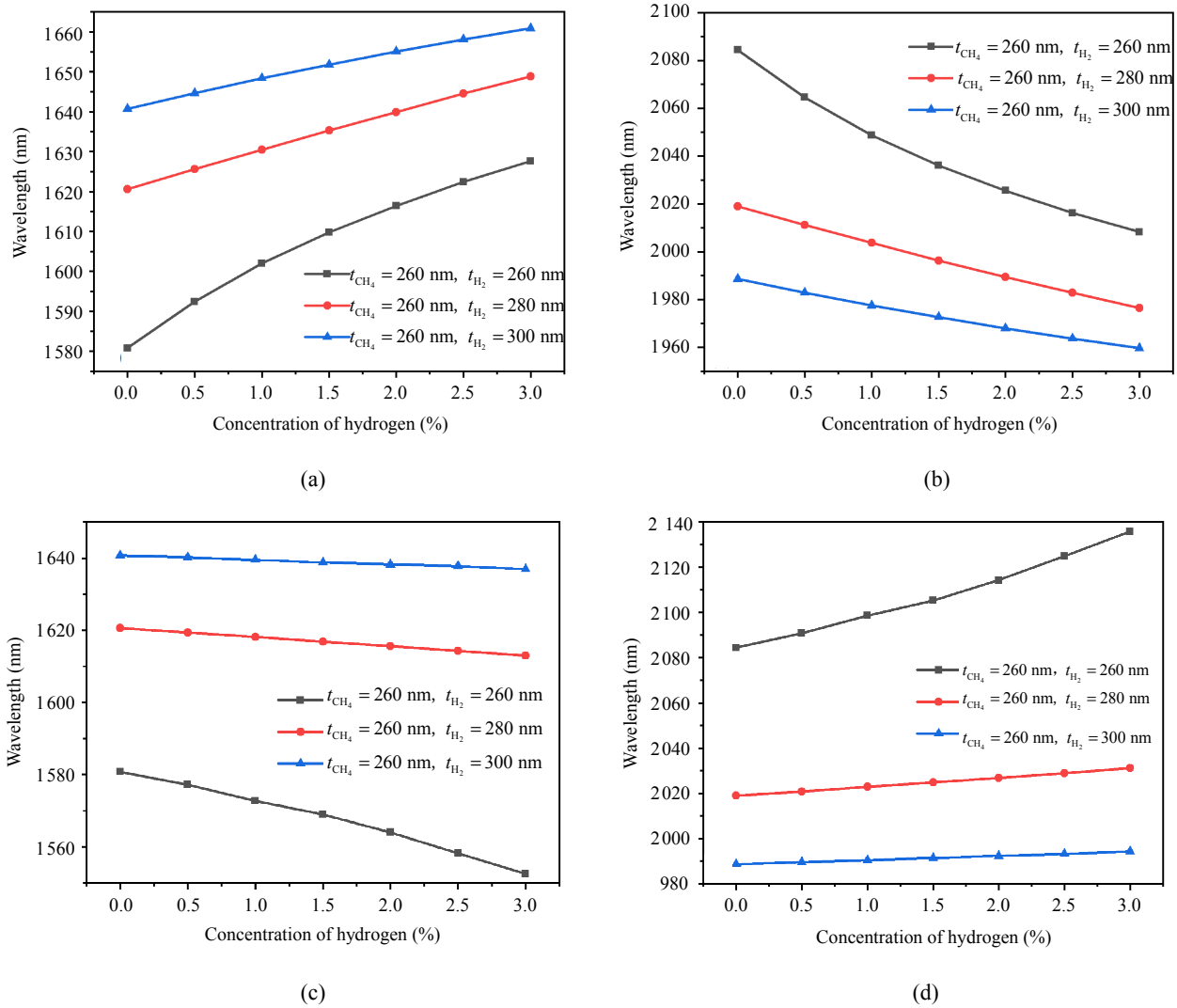

Fig. 4 Anti-Stokes peak wavelength shift curves (a) and Stokes peak wavelength shift curves (b) with the variation of the hydrogen concentration; anti-Stokes peak wavelength shift curves (c) and Stokes peak wavelength shift curves (d) with the variation of the methane concentration.

Under the same conditions, the gain peak curves with the variations of the methane concentration can be obtained by keeping the hydrogen concentration constant at 0% and changing the methane concentration from 0% to 3.5%. Figure 3(b) shows the gain peak curves of the methane concentration at 0% – 2%. The peak value decreases with an increase in the hydrogen gas-sensitive film thickness, and the methane concentration also has little effect on the peak value. It can be clearly seen from Figs. 4(c) and 4(d) that each group of the Stokes peaks moves to the short-wave direction, while that of the anti-Stokes peaks moves to the long-wave direction with the augment of the hydrogen gas-sensitive film thickness when the methane gas-sensitive film thickness and methane concentration are constant, which is consistent with those in Fig. 3(a). However, the difference is that anti-Stokes peaks have the blue-shift and the Stokes peaks have the red-shift when the methane volume fraction is varied by 0.5%. Although the peak offsets are reduced, the linearities remain basically unchanged. Considering the sensitivity and linearity comprehensively, we finally choose the hydrogen gas-sensitive film thickness as 280 nm.

Then, the influences of the methane gas-

sensitive film thickness on the sensitivity have been studied. The thickness of the hydrogen gas-sensitive film is kept at 280 nm, and the methane gas-sensitive film thickness is changed from 260 nm to 300 nm with a step length of 20 nm. Firstly, we research the effects on the hydrogen sensitivity. The variations of the Stokes and anti-Stokes gain peaks under different hydrogen concentrations (0% – 2%) are plotted in Fig. 5(a). We can see that the gain peak values are almost constant while the wavelength positions are changed. It can be seen from Figs. 6(a) and 6(b) that the anti-Stokes gain peaks of each group move to the long-wave direction, and the Stokes gain peaks move to the short-wave direction as the methane gas-sensitive film thickness increases when the hydrogen concentration is constant. The Stokes peaks blueshifted, but the anti-Stokes peaks are redshifted with increasing the hydrogen concentration. The offsets of both all decrease and the linearities also go down. The conclusions what we obtain here are also consistent with those in Fig. 3(a), except for the linearity.

Secondly, we study the effects on the sensitivity of methane under the same conditions as those in Fig. 5(a), which is shown in Fig. 5(b). The methane gas-sensitive film thickness and the methane concentration have little effect on the gain peak value, but only the peak wavelengths are changed. The wavelength shifts are illustrated in Figs. 6(c) and 6(d). We find that with the augment of the methane gas-sensitive film thickness, the movement direction of the anti-Stokes and Stokes gain peaks of each group is the same as that in Fig. 5(a) when the methane concentration is constant. However, the movements of the Stokes and anti-Stokes peaks are just opposite to those in Fig. 5(a) with the augment of the methane concentration. The offsets of the Stokes and anti-Stokes peaks all decrease, and the linearities are almost constant. Considering the sensitivity and linearity comprehensively, we finally choose the methane gas-sensitive film thickness of 260 nm. In conclusion, when the gas concentrations are constant, the anti-Stokes gain peaks of each group move to the long-wave direction, and Stokes gain peaks move to the short-wave direction with the gas-sensitive film thickness increases. Both the offsets decrease. When the thickness of the gas-sensitive film is fixed, with the augment of the hydrogen concentration, the Stokes peaks are blueshifted and anti-Stokes peaks are redshifted. However, the Stokes peaks are redshifted and the anti-Stokes peaks are blueshifted with increasing the methane concentration. The displacements of the Stokes and anti-Stokes peaks are just inverse.

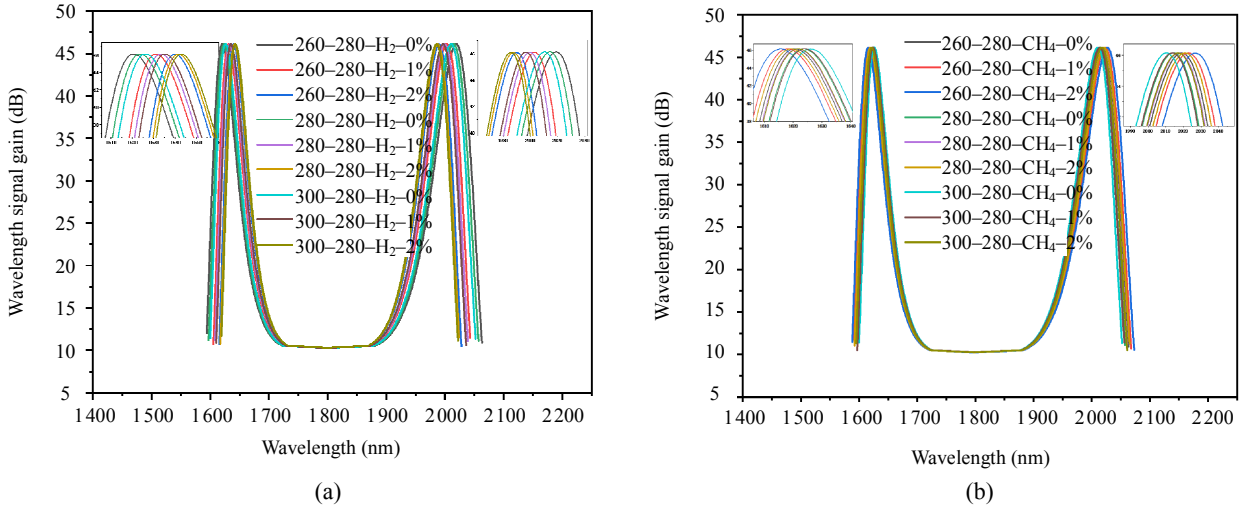

Fig. 5 Stokes and anti-Stokes gain spectrum curves with the variation of the hydrogen concentration (a) and Stokes and anti-Stokes gain spectrum curves with the variation of the methane concentration (b).

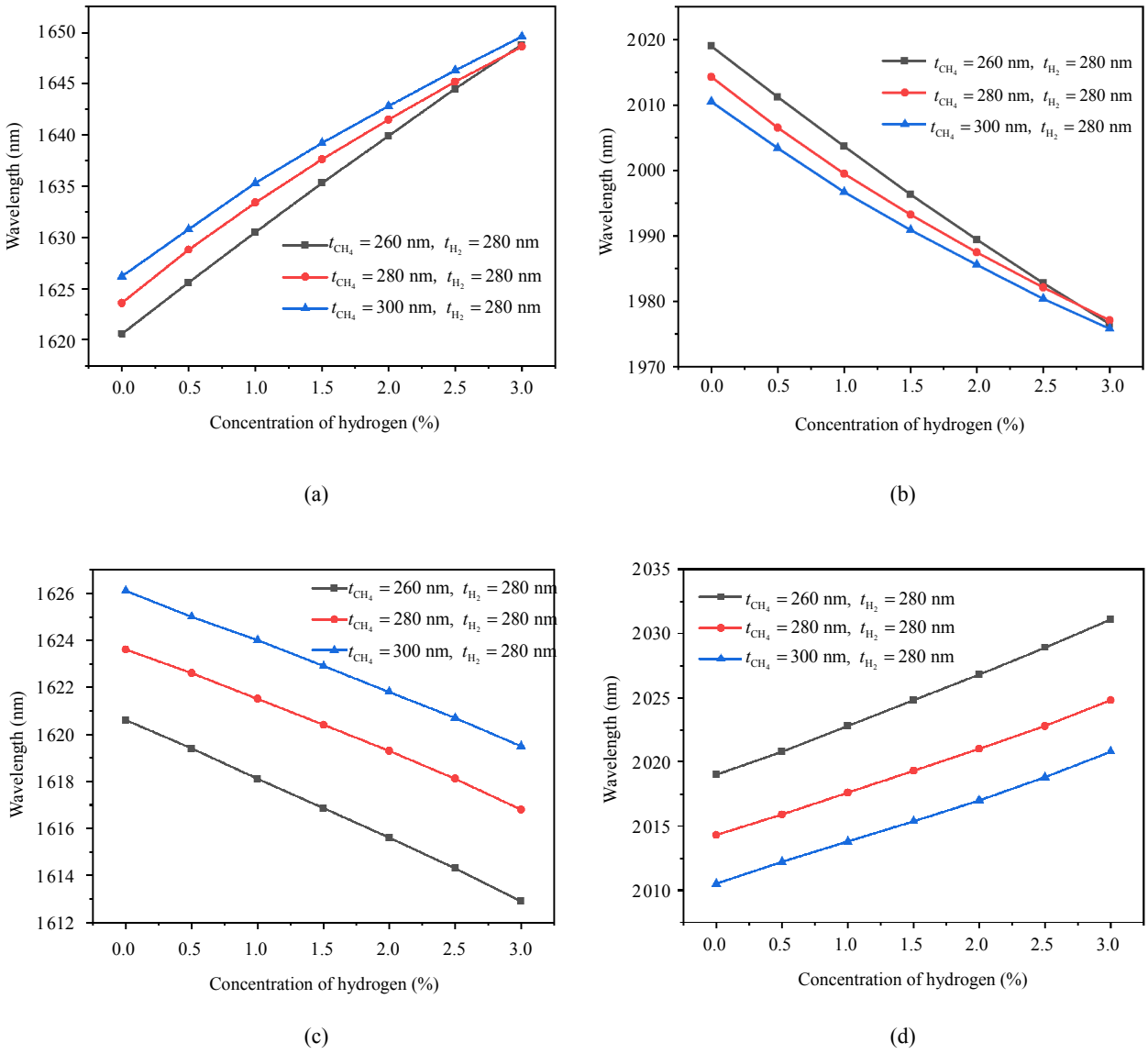

Fig. 6 Anti-Stokes peak wavelength shift curves (a) and Stokes peak wavelength shift curves (b) with the variation of the hydrogen concentration; anti-Stokes peak wavelength shift curves (c) and Stokes peak wavelength shift curves (d) with the variation of the methane concentration.

The specific sensitivities vary with the gas-sensitive film thicknesses are shown in Fig. 7. The sensitivities here are just the Stokes sensitivities of methane and hydrogen. It can be concluded that the sensitivity decreases with an increase in the gas-sensitive film thickness. The reason is that the coupling between the evanescent waves of core guiding-light and the external analyte is reduced, which weakens the SPR effect and thus lowers the peak offset of the FWM. The overall sensitivity variations are listed in Table 1. Taking the above factors into consideration, the numerical values, as shown in Table 2, are selected as the optimal structural parameters of the sensor structure.

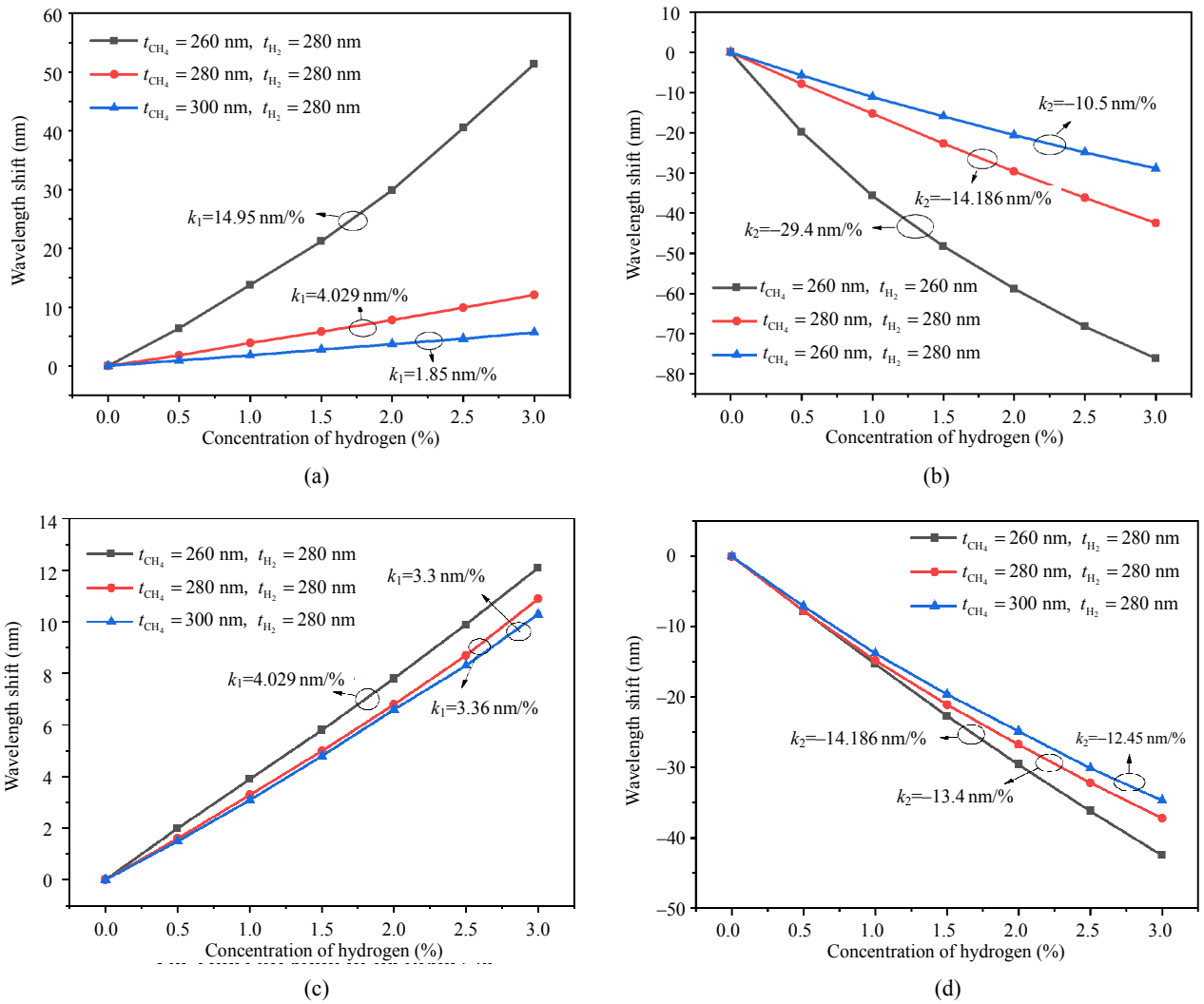

Fig. 7 Specific Stokes sensitivities vary with the gas-sensitive film thicknesses: (a) Stokes methane sensitivity curves and (b) Stokes hydrogen sensitivity curves with the thickness of the hydrogen gas-sensitive film; (c) Stokes methane sensitivity curves and (d) Stokes hydrogen sensitivity curves with the thickness of the methane gas-sensitive film.

Table 1 Influence of the gas-sensitive film thickness on sensitivity.

t_{CH_4} (nm)	t_{H_2} (nm)	Sensitivity (nm/%)					
		CH_4			H_2		
		k_1	k_3	Linear	k_2	k_4	Linear
260	260	14.95	–8.4	0.99	–29.4	17.8	0.975
	280	4.029	–2.557	0.999	–14.19	9.414	0.999
	300	1.85	–1.3	0.999	–10.5	7	0.999
280	260	11.2	–6.45	0.996	–24.85	15.35	0.97
	280	3.38	–2.15	0.998	–13.4	8.95	0.994
	300	1.75	–1.225	0.999	–9.8	6.85	0.996
300	260	9.35	–5.55	0.998	–21.9	13.65	0.968
	280	3.3	–2.2	0.999	–12.45	8.3	0.992
	300	1.6	–1.1	0.999	–9.35	6.55	0.994

Table 2 Structural parameters of the sensor.

Λ	d	h	d_{CH_4}	d_{H_2}	t_{CH_4}	t_{H_2}
8 μm	3.2 μm	9.6 μm	40 nm	40 nm	260 nm	280 nm

According to the formula in Section 2, we know that the variations of β_2, β_4, and γ will affect the FWM gain curve. The curves of these parameters with the variation of the gas concentration are shown in Figs. 8(a), 8(b), and 8(c). With different methane concentrations, the calculated PCF parameters β_2, β_4, and γ vary linearly from $3.308\ 75\times10^{-3}$ ps^2/m to $2.956\ 62\times10^{-3}$ ps^2/m, from $-2.000\ 97\times10^{-5}$ ps^4/m to -1.64466×10^{-5} ps^4/m, and from 0.024572253 W$^{-1}\cdot$m^{-1} to 0.024 572 047 W$^{-1}\cdot$m^{-1}, respectively. Through these parameters, we obtain the gain curves of the FWM, as shown in Fig. 9(a). As can be seen, the Stokes peak has a red-shift and the anti-Stokes peak has a blue-shift with the augment of the methane concentration. The specific peak wavelength movements are described in Fig. 10(a). The Stokes and anti-Stokes lines shift from 2 019 nm to 2 031.1 nm and from 1 620.6 nm to 1 612.9 nm, respectively. Figure 10(b) indicates that the linear fitting degree of the Stokes and anti-Stokes peaks can reach 99.9%. The sensitivity coefficient of methane can reach to $k_1 = 4.029$ nm/% and $k_3 = -2.557$ nm/%, respectively.

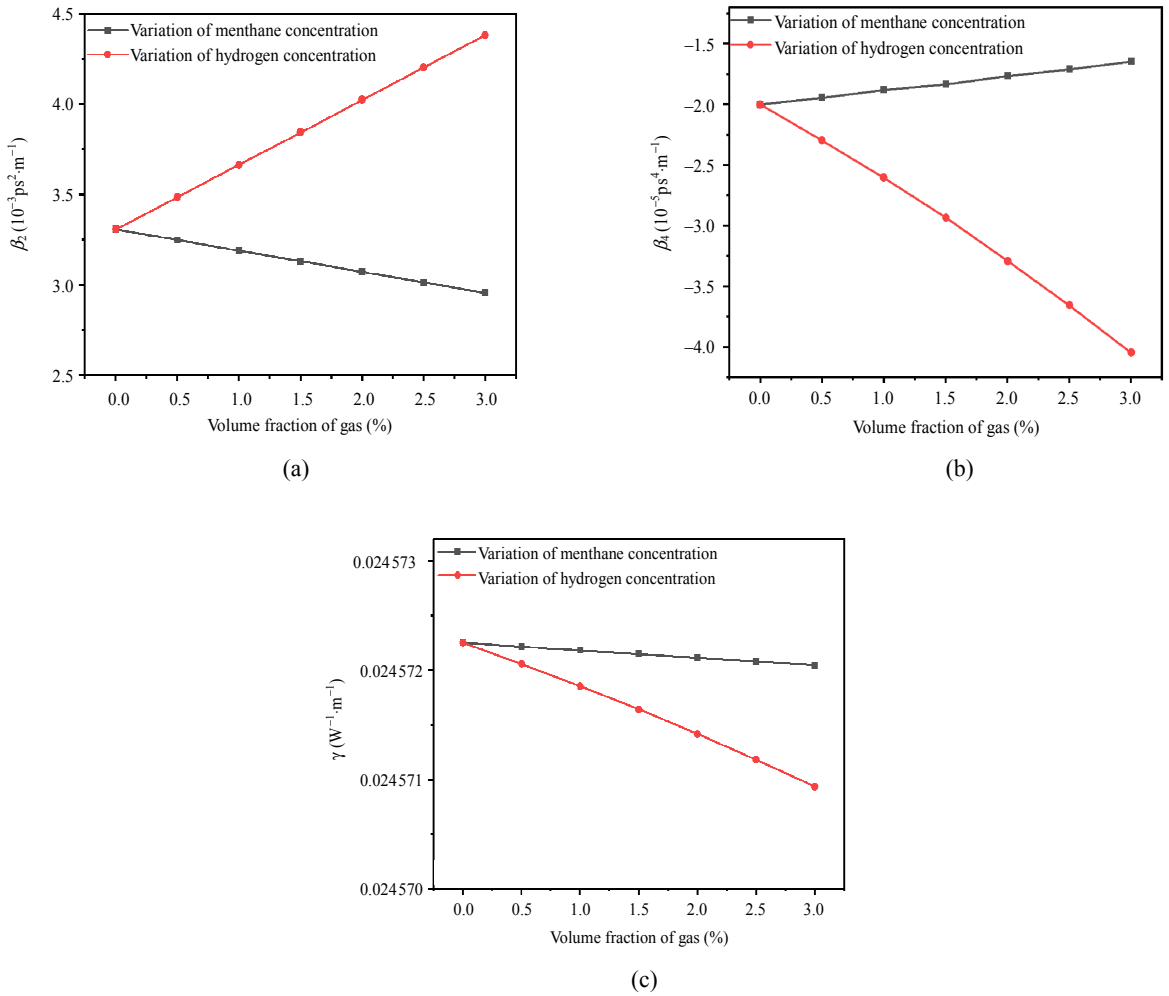

Fig. 8 Plots of the variation of (a) β_2, (b) β_4, and (c) γ with the gas concentrations.

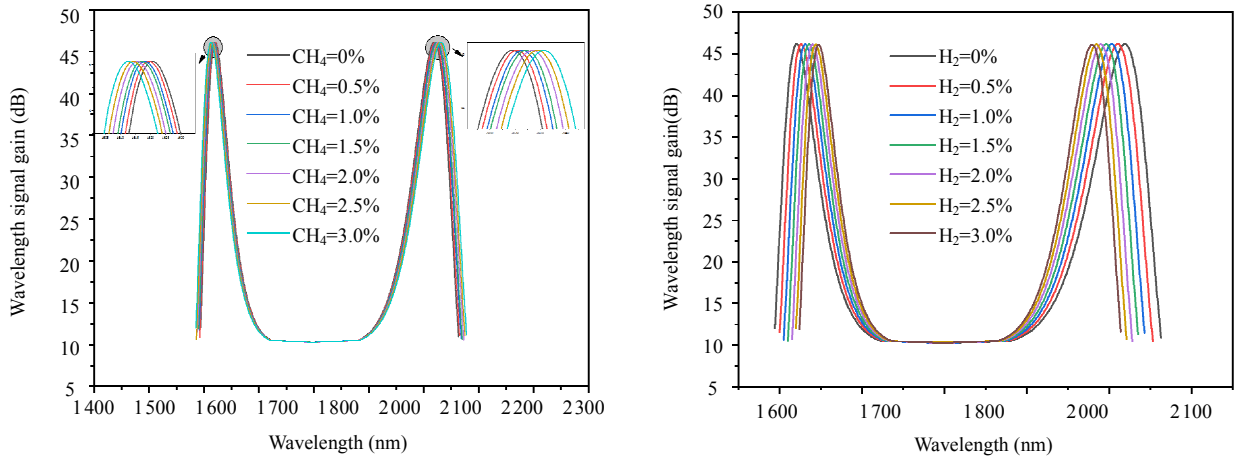

Fig. 9 Stokes and anti-Stokes gain curves affected by gas concentrations under optimal parameters: (a) Stokes and anti-Stokes gain spectrum curves when the methane concentration is 0% – 3% and (b) Stokes and anti-Stokes gain spectrum curves with the variation of the hydrogen concentration.

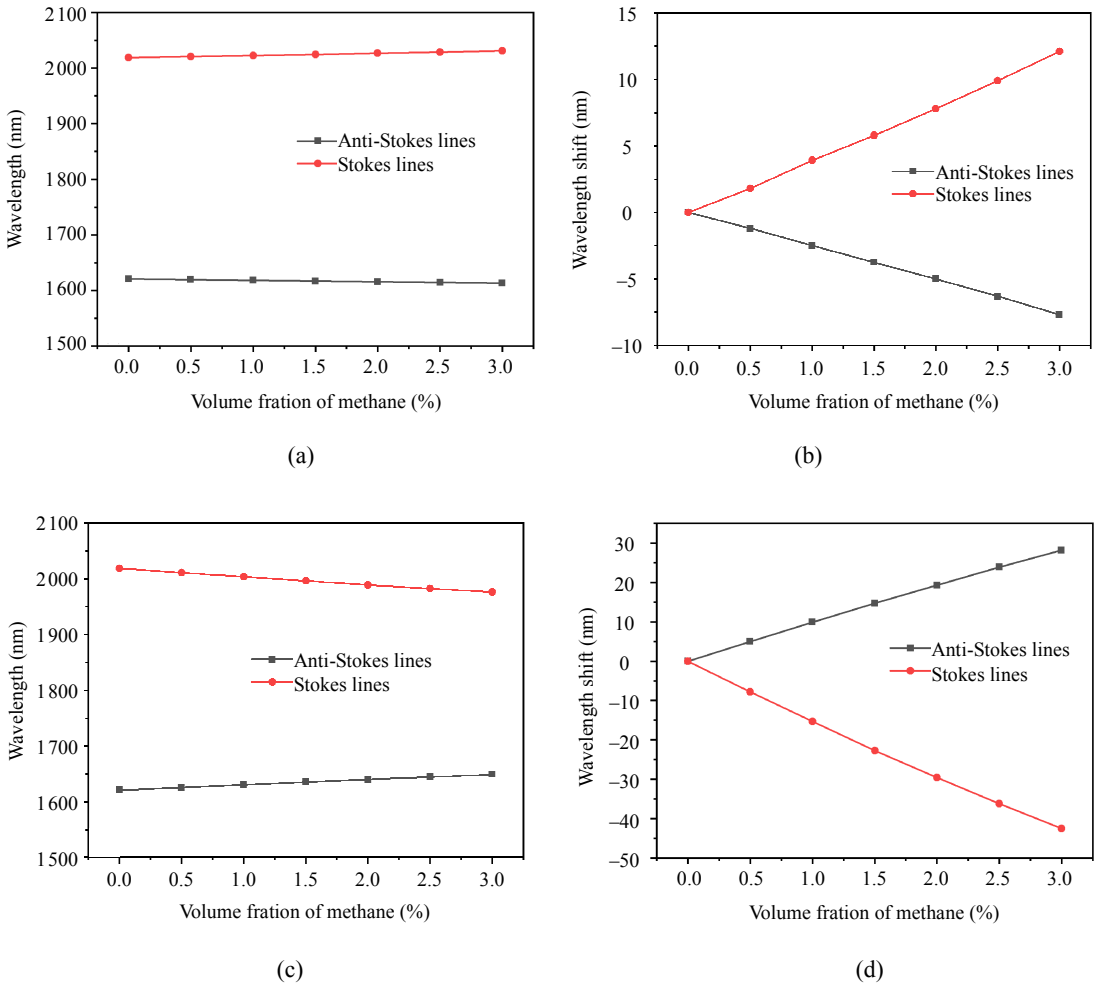

Fig. 10 Stokes and anti-Stokes peak wavelength shift curves and sensitivity fitting affected by gas concentrations under optimal parameters: (a) peak wavelength shift curves and (b) sensitivity fitting curves with methane concentrations; (c) peak wavelength shift curves and (d) sensitivity fitting curve with hydrogen concentrations.

Similarly, it can also be found from Fig. 8 that the PCF parameters vary with hydrogen concentrations. From Figs. 8(a), 8(b), and 8(c), β_2 shifts from $3.308\ 75\times10^{-3}$ ps^2/m to $4.381\ 64\times10^{-3}$ ps^2/m, β_4 varies from $-2.000\,97\times10^{-5}$ ps^4/m to $-4.045\,74\times10^{-5}$ ps^4/m, and γ changes from 0.024 572 253 W$^{-1}\cdot$m^{-1} to 0.024 570 935 W$^{-1}\cdot$m^{-1}. Figure 9(b) shows the obtained Stokes and anti-Stokes gain curves. In contrast to Fig. 9(a), as the concentration of hydrogen increases, the Stokes peak has a blue-shift from 2 019 nm to 1 976.5 nm and the anti-Stokes peak has a red-shift from 1620.6 nm to 1648.8 nm. The sensitivities of hydrogen are $k_2=-14.186$ nm/% and $k_4=9.414$ nm/%, respectively. Their linearity can also reach up to 99.9%.

In addition, Fig. 10 shows that the variations of the gas concentration and the wavelength shifts of the Stokes and anti-Stokes gain peaks are linear. Hence, the variations of methane and hydrogen concentrations can be measured simultaneously by using a 2×2 sensitivity matrix [24], where $k_1=4.029$ nm/% and $k_3=-2.557$ nm/% are the Stokes and anti-Stokes sensitivity coefficients of methane, respectively, and $k_2=-14.186$ nm/% and $k_4=9.414$ nm/% are the Stokes and anti-Stokes sensitivity coefficients of hydrogen, respectively. When the concentrations of methane and hydrogen change, the variations in the concentration of methane and hydrogen can be calculated by substituting the peak shifts $\Delta\lambda_1$ and $\Delta\lambda_2$ into (12), where $\Delta\lambda_1$ and $\Delta\lambda_2$ are the peak movements of the Stokes and anti-Stokes gains, respectively.

$$\begin{bmatrix}\Delta C_{CH_4}\\ \Delta C_{H_2}\end{bmatrix}=\begin{bmatrix}k_1 & k_2\\ k_3 & k_4\end{bmatrix}^{-1}\begin{bmatrix}\Delta\lambda_1\\ \Delta\lambda_2\end{bmatrix}. \tag{12}$$

We can define a two-dimensional parameter $\left(C_{CH_4}/\%,\ C_{H_2}/\%\right)$ to represent the gas mixture. Here, we select $(0.6\%,\ 1.5\%)$ as the initial state and $(1.8\%,\ 2.5\%)$ as the final state to verify the feasibility of the proposed measurement method. Figure 11 shows the FWM gain spectra of the initial and final states. The Stokes peak blueshifts and the anti-Stokes peak redshifts with increasing methane and hydrogen concentrations. From Fig. 11, we can obtain $\Delta\lambda_1=-10.06$ nm and $\Delta\lambda_2=6.82$ nm. After substituting it into (12), we can determine that the result is $(1.83\%,\ 2.56\%)$ within the margin of error. It is vigorously proved that the proposed structure can accurately measure methane and hydrogen concentrations simultaneously.

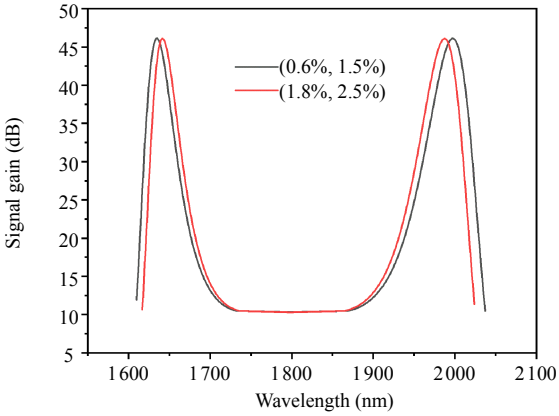

Fig. 11 FWM gain spectra of the initial and final states.

In addition, the resolution of the dual-parameter sensor proposed in this paper can be defined as (13) [25], where ΔC demonstrates the variation of the methane or hydrogen concentration, $\Delta\lambda_{min}$ is the minimum spectral resolution of 0.1 nm, and $\Delta\lambda_{peak}$ is the resonance wavelength shift. When the concentration of methane or hydrogen changes by 0.05%, the calculated methane and hydrogen resolutions are $1.25\times10^{-2}\%$ and $7.14\times10^{-3}\%$, respectively.

$$R=\Delta C\times\frac{\Delta\lambda_{min}}{\Delta\lambda_{peak}}. \tag{13}$$

Table 3 shows some sensors based on the photonic crystal fiber published in recent years. By comparison, the D-shaped PCF-SPR sensor proposed in this paper has obvious advantages in terms of both the sensitivity and linearity. Meanwhile, this is a new study of FWM gas sensing

combined with the SPR effect in the non-silicon D-PCF, expanding the gas detection method.

Table 3 Comparison of photonic crystal fiber sensors.

Type	Methane sensitivity (nm/%)	Hydrogen sensitivity (nm/%)	Linear	Reference
LPFG	2.5	/		[26]
Side-holes	4.6	/	0.999	[27]
PCF loop mirror	/	–1.12		[28]
Modal interferometer	/	1.28	0.998	[29]
PCF-SPR	–1.99	–0.19	0.999	[8]
Waveguide	1.7	0.13	0.999	[30]
This paper	4.03	–14.19	0.999	

5. Conclusions

Many traditional D-PCF sensors adopt the loss spectrum analysis method, which needs to be combined with other methods (coupling or interference method) to realize double-parameter detection. Since the transmission loss of the quartz fiber is larger in the near infrared region, we propose a tellurite PCF-SPR methane and hydrogen sensor based on the FWM effect. We use tellurite glass as the substrate, and plate the gold film and hydrogen-sensitive film onto the polished surface of the D-PCF. Then, we select another air hole of the inner cladding to be coated with the gold film and methane-sensitive film to form the second sensing channel. The peak shifts of the Stokes and anti-Stokes spectra caused by the variation of the gas concentration can be measured by the FWM effect, and the concentration of methane and hydrogen in the mixed gas can be accurately measured. It is found that the SPR effect can increase the peak shifts of the Stokes and anti-Stokes spectra and enhance the gas sensitivities. In addition, the peak displacements of the Stokes and anti-Stokes spectra are basically unchanged as the fiber length shortens, which is conducive to the construction of compact or ultra-compact embedded FWM sensors.

Acknowledgment

Thanks to the State-Level Experimental Teaching Demonstration Centre for Electrotechnics and Electronics in CUMT for providing the computing servers.

This research was funded by the National Natural Science Foundation of China (Grant No. 51874301) and Primary Research & Development Plan of Xuzhou City (Grant No. KC20162).

References

[1] M. De and V. K. Singh, "Wide range refractive index sensor using a birefringent optical fiber," *Optical and Quantum Electronics*, 2021, 53: 198–213.

[2] H. R. Wang, W. Zhang, C. Chen, S. F. Tang, and H. Liu, "A new methane sensor based on compound film-coated photonic crystal fiber and Sagnac interferometer with higher sensitivity," *Results in Physics*, 2019, 15: 102817.

[3] H. Liu, H. Li, Q. Wang, M. Wang, Y. Ding, and C. Zhu, "Simultaneous measurement of temperature and magnetic field based on surface plasmon resonance and Sagnac interference in a D-shaped photonic crystal fiber," *Optical and Quantum Electronics*, 2018, 50(11): 392–402.

[4] H. Liu, H. Li, Q. Wang, M. Wang, Y. Ding, C. Zhu, *et al.*, "Temperature-compensated magnetic field sensor based on surface plasmon resonance and directional resonance coupling in a D-shaped photonic crystal fiber," *Optik*, 2018, 158: 1402–1409.

[5] Y. L. Lo, C. H. Chuang, and Z. W. Lin, "Ultrahigh sensitivity polarimetric strain sensor based upon D-shaped optical fiber and surface plasmon resonance technology," *Optics Letters*, 2011, 36(13): 2489–2491.

[6] S. Sen, M. Abdullah-Al-Shafi, A. S. Sikder, M. S. Hossain, and M. M. Azad, "Zeonex based decagonal photonic crystal fiber (D-PCF) in the terahertz (THz) band for chemical sensing applications," *Sensing and Bio-Sensing Research*, 2020, 31: 100393.

[7] N. Luan and J. Yao, "Refractive index and

temperature sensing based on surface plasmon resonance and directional resonance coupling in a PCF," *IEEE Photonics Journal*, 2017, 9(2): 1–7.

[8] H. Liu, M. Wang, Q. Wang, H. Li, Y. Ding, and C. Zhu, "Simultaneous measurement of hydrogen and methane based on PCF-SPR structure with compound film-coated side-holes," *Optical Fiber Technology*, 2018, 45: 1–7.

[9] N. Nallusamy, R. V. J. Raja, N. Arzate, and I. Torres-Gómez, "Simultaneous measurement of salinity and temperature in gold-coated D-shaped photonic crystal fiber using four-wave mixing technique," *IEEE Sensors Letters*, 2018, 2(2): 1–4.

[10] G. Steinmeyer and J. S. Skibina, "Supercontinua: entering the mid-infrared," *Nature Photonics*, 2014, 8(11): 814–815.

[11] J. S. Wang, E. M. Vogel, E. Snitzer, "Tellurite glass: a new candidate for fiber devices," *Optical Materials*, 1994, 3(3): 187–203.

[12] G. Qin, X. Yan, C. Kito, M. Liao, T. Suzuki, A. Mori, *et al.*, "Zero-dispersion-wavelength-decreasing tellurite microstructured fiber for wide and flattened supercontinuum generation," *Optics Letters*, 2010, 35(2): 136–138.

[13] Y. Sun, X. Yan, F. Wang, X. Zhang, S. Li, T. Suzuki, *et al.*, "Theoretical investigation of an alcohol-filled tellurite photonic crystal fiber temperature sensor based on four-wave mixing," *Sensors*, 2020, 20(4): 1007.

[14] X. Chen, Y. Xin, X. Zhang, F. Wang, S. Li, T. Suzuki, *et al.*, "Theoretical investigation of mid-infrared temperature sensing based on four-wavemixing in a CS_2-filled GeAsSeTe microstructured optical fiber," *IEEE Sensors Journal*, 2021, 21(9): 10711–10718.

[15] S. Masuzawa, S. Okazaki, Y. Maru, and T. Mizutani, "Catalyst-type-an optical fiber sensor for hydrogen leakage based on fiber Bragg gratings," *Sensors Actuators B*, 2015, 217: 151–157.

[16] M. Fisser, R. A. Badcock, P. D. Teal, and A. Hunze, "High-sensitivity fiber-optic sensor for hydrogen detection in gas and transformer oil," *IEEE Sensors Journal*, 2019, 19(9): 3348–3357.

[17] S. Pitois and G. Millot, "Experimental observation of a new modulational instability spectral window induced by fourth-order dispersion in a normally dispersive single-mode optical fiber," *Optics Communications*, 2003, 226(1–6): 415–422.

[18] Y. Geng, L. Wang, Y. Xu, A. G. Kumar, X. Tan, and X. Li, "Wavelength multiplexing of four-wave mixing based fiber temperature sensor with oil-filled photonic crystal fiber," *Optics Express*, 2018, 26(21): 27907–27916.

[19] G. P. Agrawal, "*Nonlinear fiber optics*," 5nd edition, Burlington: Academic Press, 2006: 275.

[20] Y. Zhao, Q. L. Wu, and Y. N. Zhang, "High-sensitive hydrogen sensor based on photonic crystal fiber model interferometer," *IEEE Transactions on Instrumentation & Measurement*, 2017, 66(8): 2198–2203.

[21] J. C. Yang, L. Zhou, X. Che, J. Huang, X. M. Li, and W. M. Chen, "Photonic crystal fiber methane sensor based on modal interference with an ultraviolet curable fluoro-siloxane nano-film incorporating cryptophane A," *Sensors Actuators B*, 2016, 235: 717–722.

[22] Z. Liu, J. An, H. Liu, S. Liu, H. Du, and X. Zhao, "Properties analysis of tellurite photonic crystal fiber filled with nematic liquid crystal," *Optik*, 2016, 9(177): 15–20.

[23] Y. F. Geng , L. Wang, X. Tan, Y. Xu, X. Hong, and X. Li, "A compact four-wave mixing-based temperature fiber sensor with partially filled photonic crystal fiber," *IEEE Sensors Journal*, 2019, 19(8): 2956–2961.

[24] H. Liu, C. Chen, H. Wang, and W. Zhang, "Simultaneous measurement of magnetic field and temperature based on surface plasmon resonance in twin-core photonic crystal fiber," *Optik*, 2019, 203: 164007.

[25] C. Liu, L. Yang, X. Lu, Q. Liu, F. Wang, J. Lv, *et al.*, "Mid-infrared surface plasmon resonance sensor based on photonic crystal fibers," *Optics Express*, 2017, 25(13): 14227–14237.

[26] J. C. Yang, L. Zhou, J. Huang, C. Tao, X. Li, and W. Chen, "Sensitivity enhancing of transition mode long-period fiber grating as methane sensor using high refractive index polycarbonate/cryptophane A overlay deposition," *Sensors Actuators B*, 2015, 207: 477–480.

[27] H. Liu, H. Wang, C. Chen, W. Zhang, B. Bai, C. Chen, *et al.*, "High sensitive methane sensor based on twin-core photonic crystal fiber with compound film-coated side-holes," *Optical and Quantum Electronics*, 2020, 52(2): 81.1–81.10.

[28] Y. N. Zhang, T. Zhou, B. Han, L. Zhang, and Q. Wu, "Simultaneous measurement of hydrogen concentration and temperature based on fiber loop mirror combined with PCF," *IEEE Sensors Journal*, 2018, 18(6): 2369–2376.

[29] Y. N. Zhang, A. Zhang, B. Han, and S. E, "A reflective hydrogen sensor based on fiber ring laser with PCF modal interferometer," *Journal of Optics*, 2018, 20(6): 065401.

[30] W. Zhang, H. R.Wang, C. Chen, S. F. Tang, and H. Liu, "Methane and hydrogen sensor based on photonic crystal waveguide," in *Ninth International Symposium on Precision Mechanical Measurements*, Chongqing, China, Nov. 13, 2019, pp. 1134315.